Electronic Supplementary Material (ESI) for Journal of Materials Chemistry A.
This journal is © The Royal Society of Chemistry 2021

## Electronic Supplementary Information for

# Establishing Structure/Property Relationships in Atomically Dispersed Co-Fe Dual Sites M-$N_x$ Catalysts on Microporous Carbon for Oxygen Reduction Reaction

Kai Wang,[a,#] Jiapeng Liu,[b,#] Zhenghua Tang,[a,c,*] Ligui Li,[a] Zheng Wang,[b] Muhammad Zubair,[d] Francesco Ciucci,[b,e,*] Lars Thomsen,[f] Joshua Wright,[g] and Nicholas M. Bedford[d,*]

[a] Guangzhou Key Laboratory for Surface Chemistry of Energy Materials and New Energy Research Institute, School of Environment and Energy, South China University of Technology Guangzhou Higher Education Mega Center, Guangzhou, Guangdong 510006, China.

E-mail: zhht@scut.edu.cn

[b] Department of Mechanical and Aerospace Engineering, The Hong Kong University of Science and Technology Hong Kong, 999077, SAR, China.

E-mail: francesco.ciucci@ust.hk

[c] Key Laboratory of Fuel Cell Technology of Guangdong Province, School of Chemistry and Chemical Engineering, South China University of Technology, Guangzhou, 510640, China

[d] School of Chemical Engineering, University of New South Wales Sydney, New South Wales, 2052, Australia.

E-mail: n.bedford@unsw.edu.au

[e] Department of Chemical and Biological Engineering, The Hong Kong University of Science and Technology, Hong Kong, 999077, SAR, China.

[f] Australian Synchrotron, ANSTO, Clayton, Victoria, 3168, Australia.

[g] Department of Physics, Illinois Institute of Technology, Chicago, Illinois, 60616, United States.

# These authors contributed equally to this work.

**Corresponding authors:**

zhht@scut.edu.cn (Z. T.);

francesco.ciucci@ust.hk (F. C.);

n.bedford@unsw.edu.au (N. M. B.).

## 1. Electrochemical measurements

Electrochemical performances were evaluated through the CHI 760E electrochemical workstation (CH Instruments, Shanghai, China) within a three-electrode system and rotating ring disk electrode (RRDE, Pine Instruments) at ambient conditions. The carbon rod was used as the counter electrode, and Ag/AgCl with 3 M KCl was employed as the reference electrode. The working electrode was prepared by dropcasting a catalyst ink on a pre-polished glass carbon electrode (GCE, 5 mm in diameter, polished using the $Al_2O_3$ powders (50 nm)). The homogeneous catalyst ink was formed as follows: typically,1 mg sample was dispersed into 0.4 mL Nafion/ethanol (the weight percentage of Nafion is 0.025%) solution by sonication for 30 min, 8 μL above catalyst ink was dropcasted onto GCE and dried at room temperature (the loading of catalyst on GCE was 0.1 mg $cm^{-2}$). All potentials were converted to reversible hydrogen electrode (RHE) via the equation of the $E_{RHE} = E_{Ag/AgCl} + 0.196 + 0.059 \times pH$. The ORR properties were evaluated by linear sweep voltammetry (LSV) and cyclic voltammetry (CV) with the potential ranging from -1.0 to 0.2 V (vs. Ag/AgCl) in $O_2$-saturated 0.1 mol $L^{-1}$ KOH electrolyte and -0.2-1.0 V (vs. Ag/AgCl) in $O_2$-saturated 0.1 mol $L^{-1}$ $HClO_4$ electrolyte at a scan rate of 10 mV $s^{-1}$ under different rotation rates (400-2500 rpm). The durability was performed via the amperometric i-t curve in $O_2$-saturated 0.1 mol $L^{-1}$ KOH and 0.1 mol $HClO_4$ electrolyte with the rotation speed of 900 rpm at potential of 0.85 V and 0.8 V(RHE) for 16 h. The yield of hydrogen peroxide ($H_2O_2$%) and numbers of electron transfer (n) at different potentials were calculated by the following **Equations S1** and **S2**:

$$n = (4I_D)/(I_D + I_R/N)$$ (**Equation S1**)

$$H_2O_2\% = (200I_R/N)/(I_D + I_R/N)$$ (**Equation S2**)

Where $I_D$ is the disk current, $I_R$ is ring current, N is the current collection efficiency of the RRDE measurement (0.37).

## 2. Zn-air battery

The Zn-air battery was self-assembled by using the polished zinc plate (The thickness is 0.2 mm, and the effective surface area is 1.0 $cm^2$) as the anode, 6 M KOH plus 0.2 M $Zn(OAc)_2{\cdot}2H_2O$ were employed as the electrolyte, the ORR catalyst loaded on hydrophobic carbon cloth was employed as the air-cathode and diffusion layer. The detail preparation method of air cathode for charge-discharge performance test as follows: 0.5 mg ORR catalyst plus 0.5 mg $IrO_2$ was first dispersed into 400 μL Nafion solution (0.5 wt.%) by sonication for 30 mins, then the above suspension was drop-casted onto the hydrophobic side of the carbon cloth with the catalyst loading of 1 mg $cm^{-2}$, in addition, the fabricating method of cathode for galvanostatic discharge capacity and discharge polarization curves were same as the charge-discharge test, the difference is that the amount of ORR catalyst is 1 mg and without $IrO_2$. The galvanostatic discharge capacity and charge-discharge performance were performed by LAND CT2001A battery program-control test system. The discharge polarization curves were recorded by CHI 760E electrochemical workstation. Power density and specific capacity of Zn-air battery was calculated follow equations:

$$Power\ density\ (mW\ cm^{-2}) = voltage \times current\ density$$ (**Equation S3)**

$$specific\ capacity\ (mAh\ g^{-1}) = \frac{current \times service\ hours}{weight\ of\ consumed\ zinc}$$ (**Equation S4)**

## 3. Characterization

The morphology structure of the samples was observed by transmission electron microscope (TEM, JEM-2010, operated at 200 kV) and field-emission scanning electron microscope (FE-SEM, Merlin, operated at 10 kV). The fine morphology structure was detected by the atomic-resolution high-angle annular dark-field scanning TEM (AR-HAADF STEM, JEM-ARM200F operated at 200 kV with cold field -emission gun and aberration corrector). The crystal structural feature of the electrocatalysts was identified by X-ray diffraction (XRD, Empyrean) with Cu $K_\alpha$ (λ =1.5406 Å) radiation at a scanning rate of 2θ= 2° $min^{-1}$. X-ray photoelectron spectra (XPS) were recorded on a Phi X-tool instrument with an Al $K_\alpha$ source (hv=1486.6 eV), the incident X-ray beam was focused on an analysis area of 200 μm in diameter with the take-off angle of 45° to the sample surface, the pass energy is 55.0 eV with the energy step of 0.1 eV. The charge correction was performed using C1s peak at 285 eV as the reference value. Inductively coupled plasmon-atomic emission spectroscopy (ICP-AES) analysis was carried out with an Agilent 5110 instrument. The specific surface area and the pore size distribution of the samples were estimated from nitrogen adsorption isotherm (Quantachrome Autosorb-iQ instrument at 77 K) by means of the Brunauer-Emmett-Teller (BET) equation and the Barrett-Joyner-Halenda (BJH) model. C and N K-edge X-ray absorption spectroscopy (XAS) measurements were performed at the SXR beamtime of the Australian Synchrotron. Powder were spread across Cu tape and

examined from 280 eV to 315 eV for C K-edge measurements and 390 to 430 eV for N K-edge measurements. All data was collected in a partial electron yield (PEY) configuration. An in-line photodiode was used as a secondary normalization source for C K-edge measurements to correct for upstream C contamination on the X-ray optics and normalization channel.[1] All data was processed and analyzed in QANT.[1] Fe and Co K-edge XAS measurements were performed at the 10-ID-B beamline of the Advanced Photon Source (APS), Argonne National Laboratory (ANL). Samples were loaded into Kapton capillaries and probed from 200 eV below the respective K-edge to approximately 1000 eV past the edge. Data was collected under a fluorescence sampling configuration. All data reduction, processing and subsequent modeling was performed using the Demeter XAS software package.[2] M-N coordination was modeled using known Fe or Co porphyrins,[3, 4] while longer range M-C distances were modeled by building a theoretical structure of Fe or Co atoms within a 2D graphitic lattice. For metal-metal modeling of CoFe-$N_x$, N atoms were replaced by corresponding metal atoms to mimic a represented metal-metal distance. All EXAFS fitting was performed using $S_0^2$ values of 0.727 and 0.798 for Co and Fe respectively, which were obtained by modeling the EXAFS of reference foils. To minimize error in CN and NND values, Debye-Waller factors were estimated from initial rounds of EXAFS fitting and then held constant. Theoretical XANES calculations were completed with FDMNES code through Finite Difference Method using self-consistent calculation (SCF).[5, 6] Lorentzian approach was used to convolute the obtained spectra.[7] Structure files used in the simulation were from simulated structures shown in **Fig. 3d** and **3f**.

High-energy X-ray diffraction (HE-XRD) were performed at the 11-ID-B beamline of the APS. All experiments were performed using an X-ray energy of 86.58 keV at a sample-to-detector distance of 220 mm. A $Q_{max}$ of 31.8 $Å^{-1}$ was obtained using an area detector. Given the need for high quality data to obtain differential pair distribution functions (dPDFs) and the relative low scattering of carbonaceous samples at higher energies, each HE-XRD patterns was collected for 30 minutes, resulting in 360 individual scans. Subsequent PDFs were obtained with established data reduction and FT mathematics[8] using the program RAD (see **Fig. S27** for HE-XRD and F(Q) data).[9] dPDFs were obtained by subtracting the NC PDF from those including atomically dispersed metals, as described from other systems elsewhere.[10]

## 4. Simulation methods

All the spin-polarized first-principle calculations were performed using the Vienna ab initio simulation package (VASP)[11, 12] with a plane-wave basis set defined by a kinetic energy cutoff of 480 eV. The projector augmented wave (PAW)[13] pseudopotentials with valence-electron configurations of $2s^22p^2$, $2s^22p^3$, $2s^22p^4$, $3p^63d^74s^1$, and $3d^84s^1$ were employed for C, N, O, Fe, and Co, respectively. The electron exchange-correlation was described using the Perdew-Burk-Ernzerhof (PBE) functional[14] under the generalized gradient approximation (GGA) scheme. The carbon support material was modeled based on a 6×6 graphene separated by more than 18 Å vacuum space along the c direction to avoid strong interactions between two adjacent layers. The Fe-$N_4$, Co-$N_4$, and Fe-$N_3$-Co-$N_3$ structures were modeled following previous studies,[15-17] as illustrated in **Fig. 3c-f.** We also simulated the slightly disordered C substrate by

creating one C vacant site and fully relaxed the structure. Both the lattice parameters and atomic positions in the substrate materials were fully relaxed using 3×3×1 k-points under the Monkhorst-Pack scheme until the energy and force converged within $10^{-5}$ eV and 0.02 eV/Å, respectively. For the relaxation of adsorbates supported on the graphene layer, only the ions were allowed to move.

To better analyze the orbital interactions between the SA metal sites and the adsorbate $O_2$ molecule, we performed single point calculations for the above structures using Gaussian 09 D.01 with PBE functional and cluster approach.[14, 18] The method of principal interacting spin orbitals[19] was employed to characterize the specific orbitals involved in the chemical reaction. Fictitious hydrogen atoms were applied to passivate the dangling bond at the boundary. The effective core potentials (ECPs) developed by Hay and Wadt with SDD[20-22] were chosen to describe Fe and Co atoms, while the 6-31G* basis set was used for C, O, H, and N atoms. The spin multiplicity was set at 5, 2, and 5 for SA Fe, SA Co, and Co-Fe dimer, respectively, for consistency with the VASP calculations.

To account for the adsorption of an $O_2$ molecule, we followed the reaction $O_2$ (g) + *→ $O_2$*, where * indicates the substrate with an active site and $O_2$* denotes the system with $O_2$ adsorbed on the substrate. The adsorption free energy can be calculated as

$$\Delta G = \Delta E + \Delta ZPE - T\Delta S = E(O_2^*) - E(O_2) - E(*) + \Delta ZPE - T\Delta S \quad (1)$$

where $E(O_2^*)$, $E(*)$, and $E(O_2)$ represent the energy of $O_2$*, the pure substrate, and the $O_2$ molecule in the gas state, respectively, ΔZPE and ΔS are differences of the zero-point energy and the entropy between the product and the reactant, respectively.

According to the formula above, a more negative ΔG means a stronger interaction between the substrate and the $O_2$ molecule. Further, the charge density difference can be calculated as $\rho_{diff} = \rho_{sys} - \rho_{substrate} - \rho_{O2}$, where $\rho_{sys}$ is the charge density of the system with $O_2$ adsorbed on the substrate, $\rho_{substrate}$ and $\rho_{O2}$ are the charge densities of the pure substrate and an $O_2$ molecule, respectively.

The ORR mechanism for the SA Fe, SA Co, and Co-Fe dimer was studied using the following 4-electron pathway:[17]

(1) $O_2\ (g) + 2H_2O\ (l) + 4e^- + * \rightarrow OOH^* + OH^- + H_2O\ (l) + 3e^-$;

(2) $OOH^* + OH^- + H_2O\ (l) + 3e^- \rightarrow O^* + 2OH^- + H_2O\ (l) + 2e^-$;

(3) $O^* + 2OH^- + H_2O\ (l) + 2e^- \rightarrow OH^{*} + 3OH^- + e^-$;

(4) $OH^* + 3OH^- + e^- \rightarrow 4OH^- + *$.

The change in Gibbs free energy (ΔG) for all the ORR steps were calculated based on the method developed by Nørskov et al.[23] At standard conditions (U = 0, pH = 0, p = 1 bar, T = 298 K), the free energy $\Delta G_0$ can be calculated as

$$\Delta G_0 = \Delta E + \Delta ZPE - T\Delta S = E(ads^*) - E(ads) - E(^*) + \Delta ZPE - T\Delta S \quad (2)$$

where E(ads*) and E(ads) represent the energy of adsorbed intermediates (e.g., OOH*, O*, and $OH^*$), and the adsorbate in the gas state. Further, the reaction free energy at a certain U can be calculated as

$$\Delta G\ (U, pH = 0, p = 1\ bar, T = 298\ K) = \Delta G_0 - eU \quad (3)$$

where U corresponds to the applied electrode potential. The free energy of $O_2(g)$ was derived as $G_{O2(g)} = 2G_{H2O(l)} - 2G_{H2} + 4.92$ eV,[23] and the free energy of $OH^-$ was calculated by $G_{OH^-} = G_{H2O(l)} - G_{H^+}$.[23] Consequently, the closer the reaction free energy at each

elementary step is to 1.23 eV at standard condition, the better ORR catalytic performance the material is.

## Supplementary Figures

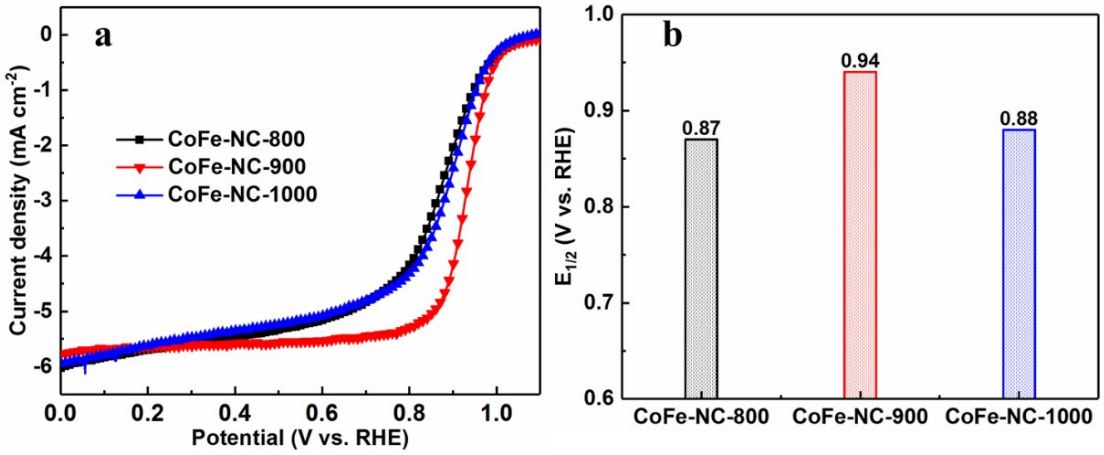


**Fig. S1.** (a) The effect of carbonization temperature on catalytic performance in 0.1 M KOH, (b) The corresponding histogram of half-wave potential.

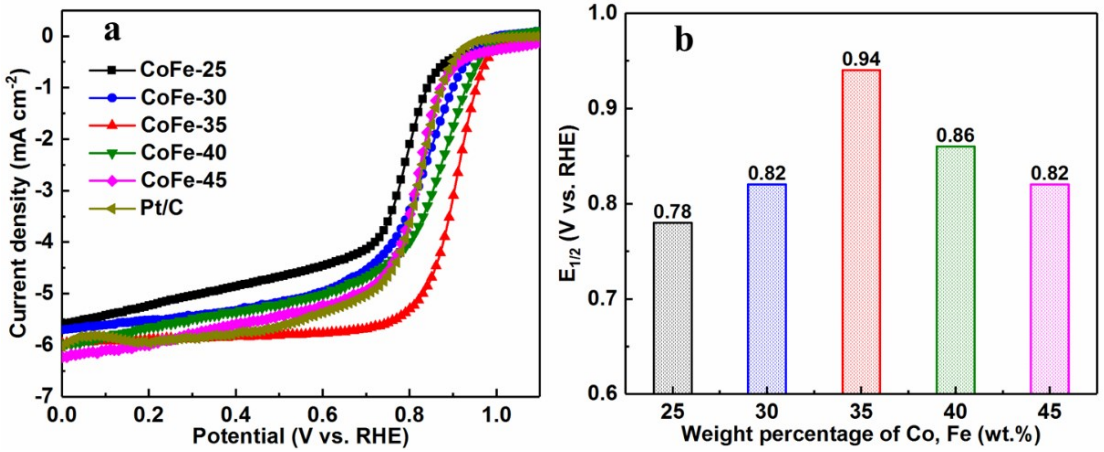


**Fig. S2.** (a) The effect of the weight percentage of Co, Fe on the catalytic activity in 0.1 M KOH, (b) The corresponding histogram of half-wave potential

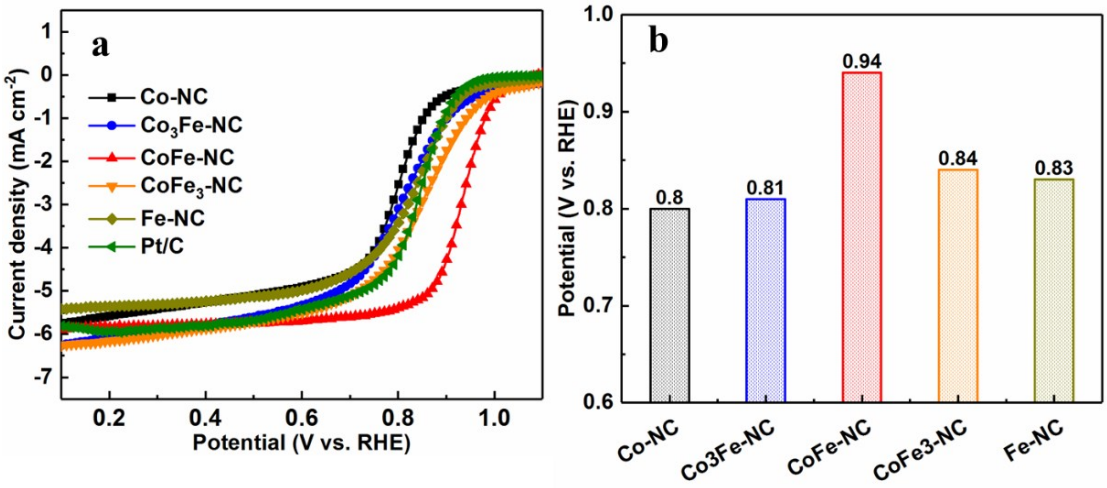


**Fig. S3.** (a) The relationship between the Co-Fe ratio of the catalysts and its electrocatalytic activity in 0.1 M KOH, (b) The corresponding histogram of half-wave potential.

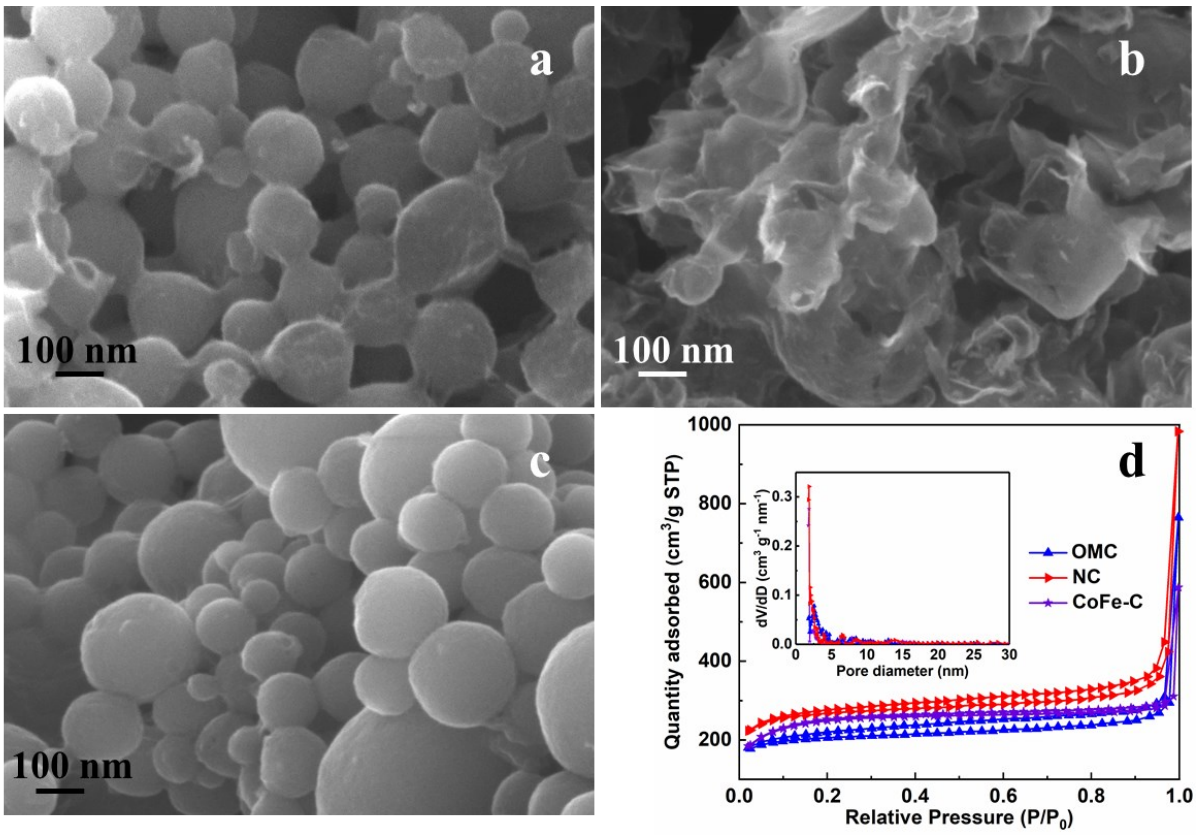

**Fig. S4.** The SEM images of (a) OMC, (b) NC and (c) CoFe-C. (d) The $N_2$ adsorption-desorption isotherms of OMC, NC, and CoFe-C; inset graph is the pore size distribution.

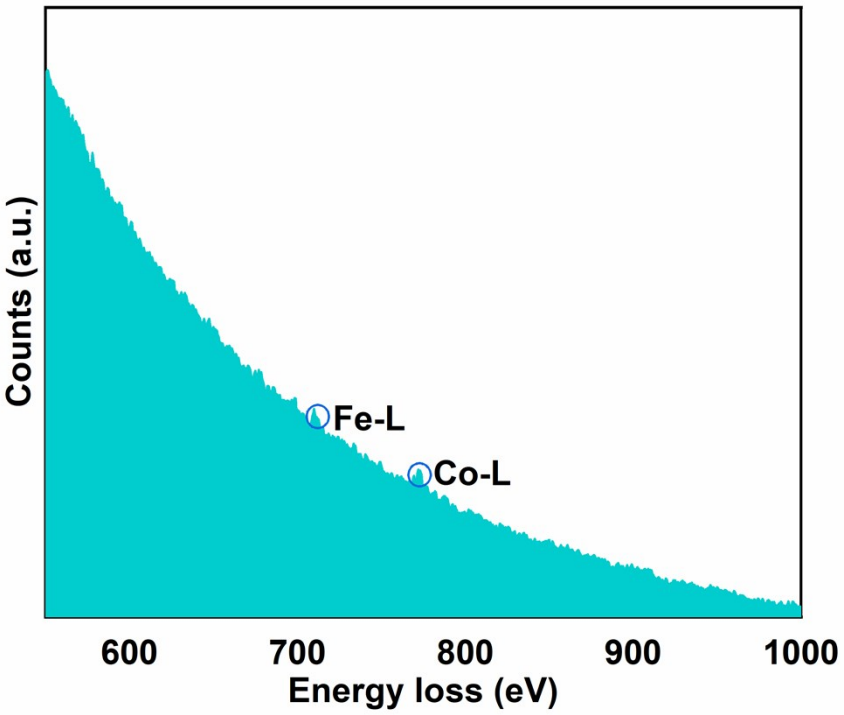


**Fig. S5**. The electron energy-loss spectroscopy (EELS) spectrum of CoFe-NC, which was taken on the white rectangle area in Fig. 2a.

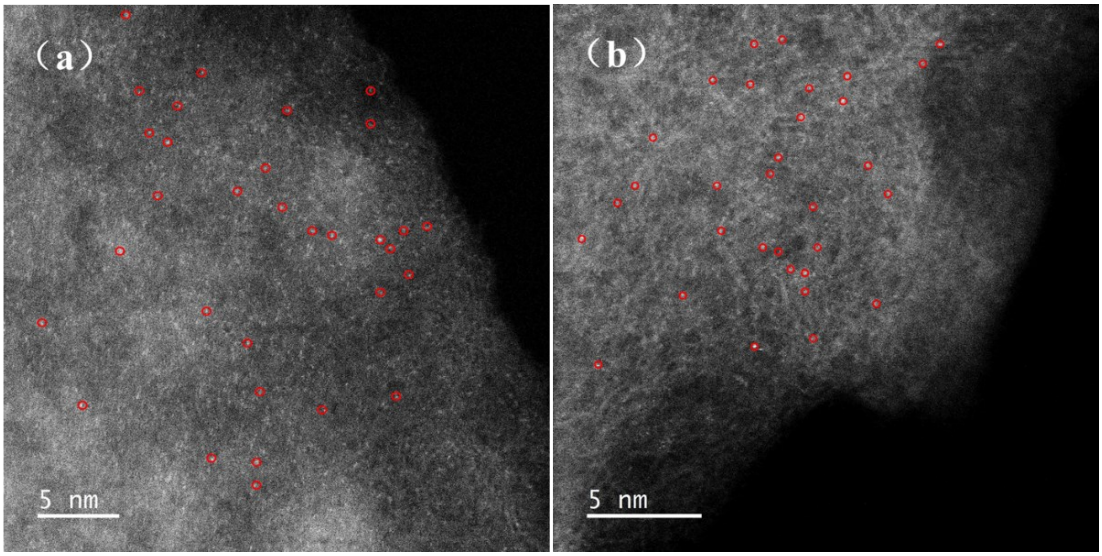

**Fig. S6.** Atomic-resolution high-angle annular dark-field scanning TEM image of (a) Co-NC, (b) Fe-NC.

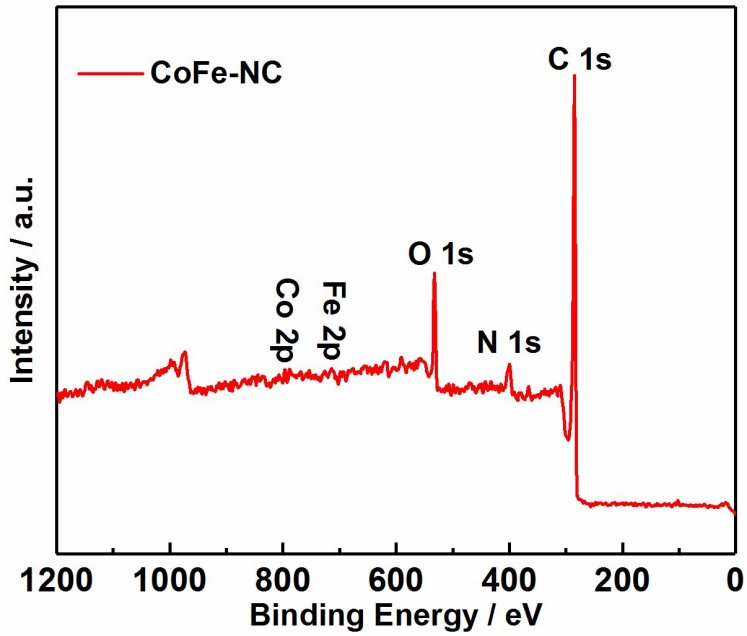


**Fig. S7.** The survey-scan XPS spectrum of CoFe-NC.

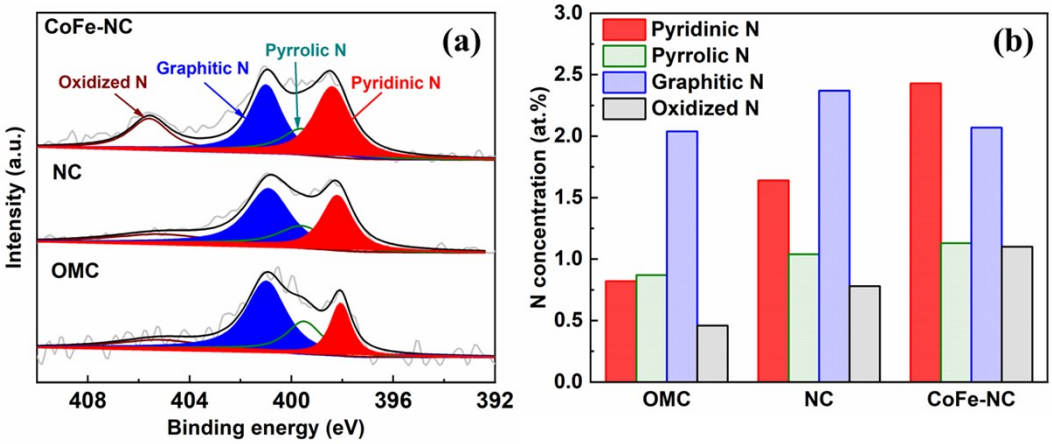


**Fig. S8** (a) High-resolution XPS N1s spectra of CoFe-NC, NC, and OMC and (b) change in the relative content of nitrogen species.

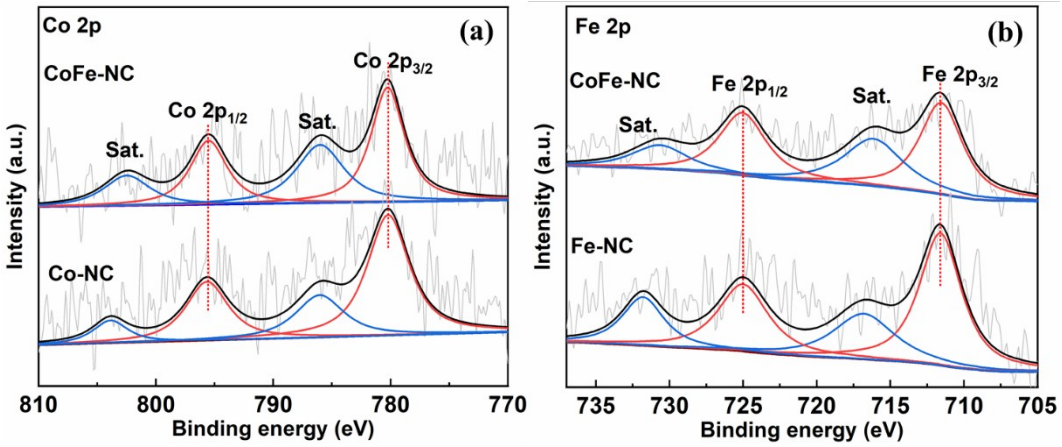


**Fig. S9.** The high-resolution XPS Co 2p (a) and Fe 2p (b) spectra of CoFe-NC, Co-NC, and Fe-NC.

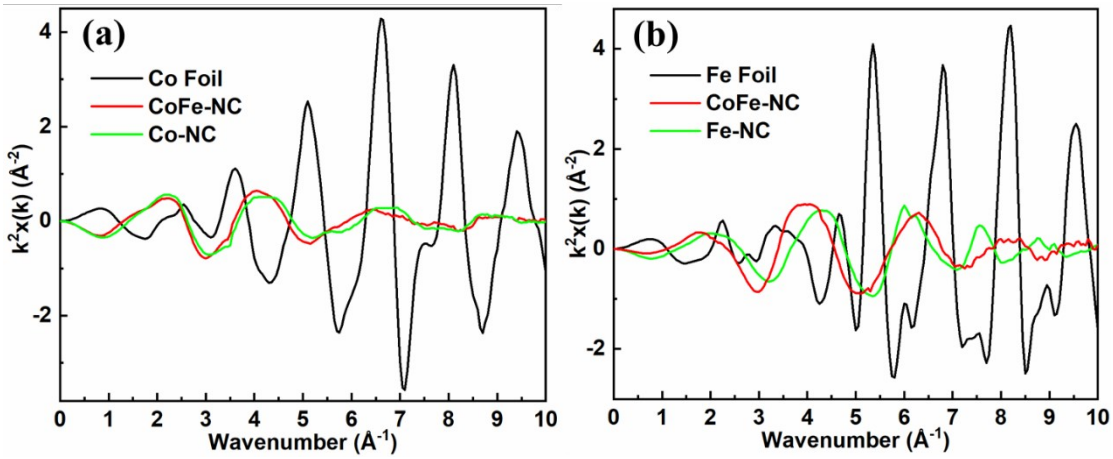


**Fig. S10** Co K-edge (a), Fe K-edge (b) FT-EXAFS of Co-NC, Fe-NC, and CoFe-NC analysis in k spaces.

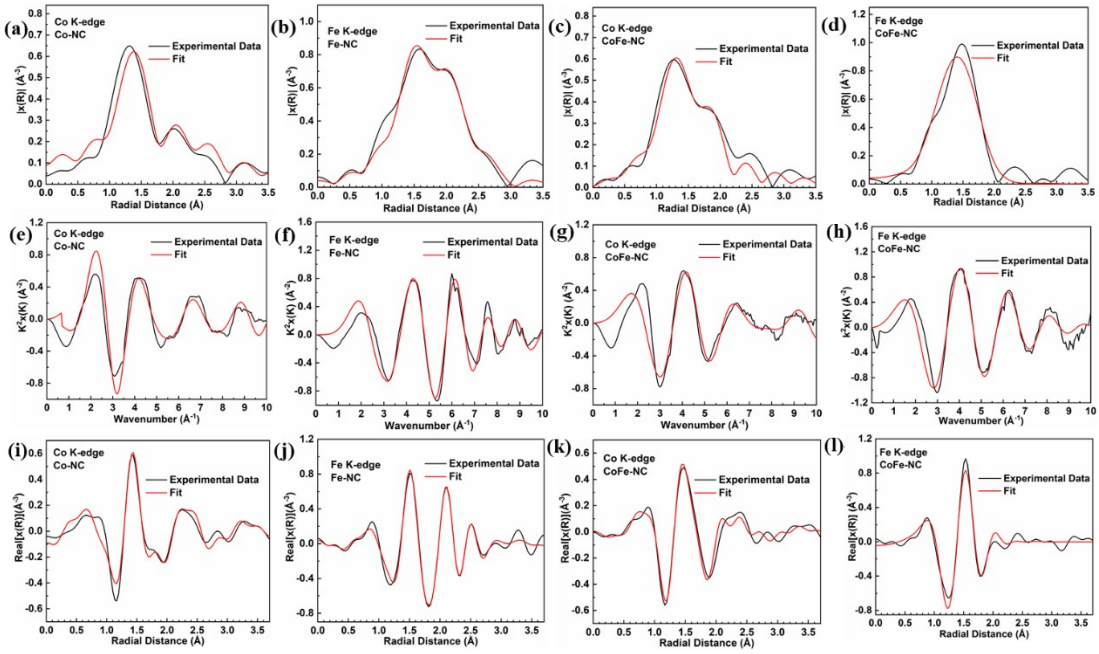


**Fig. S11** Co K-edge and Fe K-edge EXAFS fitting curves of Co-NC (a, e, i), Fe-NC (b, f, j) and CoFe-NC (c, g, k, d, h, l) at R, $k^2$ and real space of R.

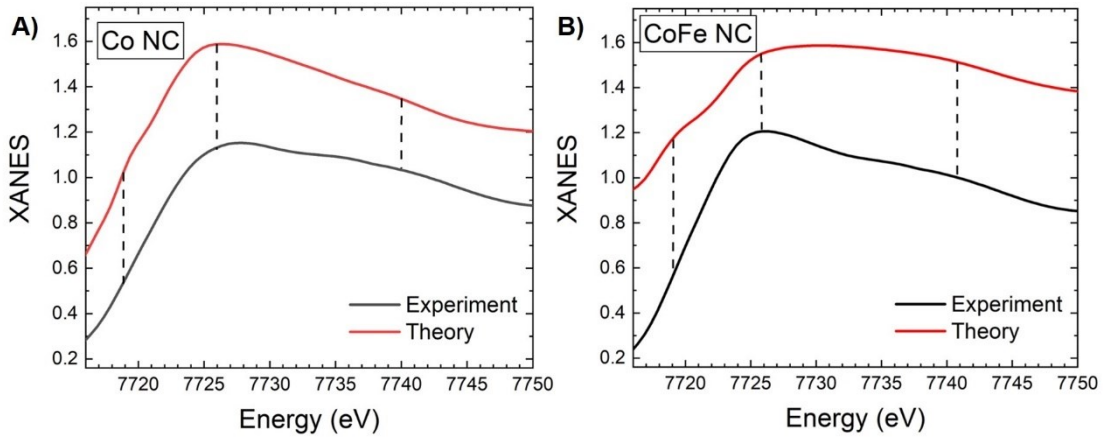


**Fig. S12** Comparison of experimental and theoretical XANES for a) Co NC and b) CoFe NC

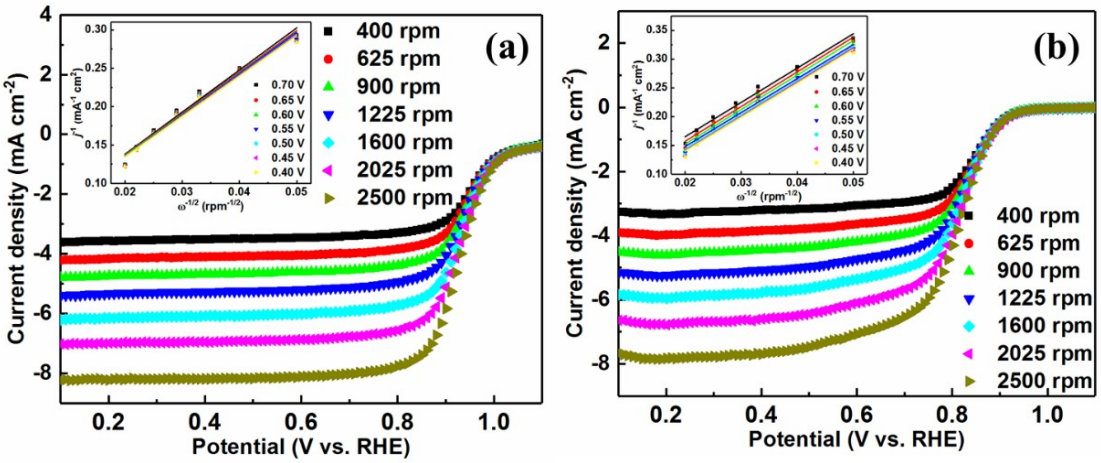


**Fig. S13.** The RDE polarization curves at different rotation rates and the inset is the corresponding K-L plots of CoFe-NC (a) and Pt/C (b) in 0.1 M KOH electrolyte.

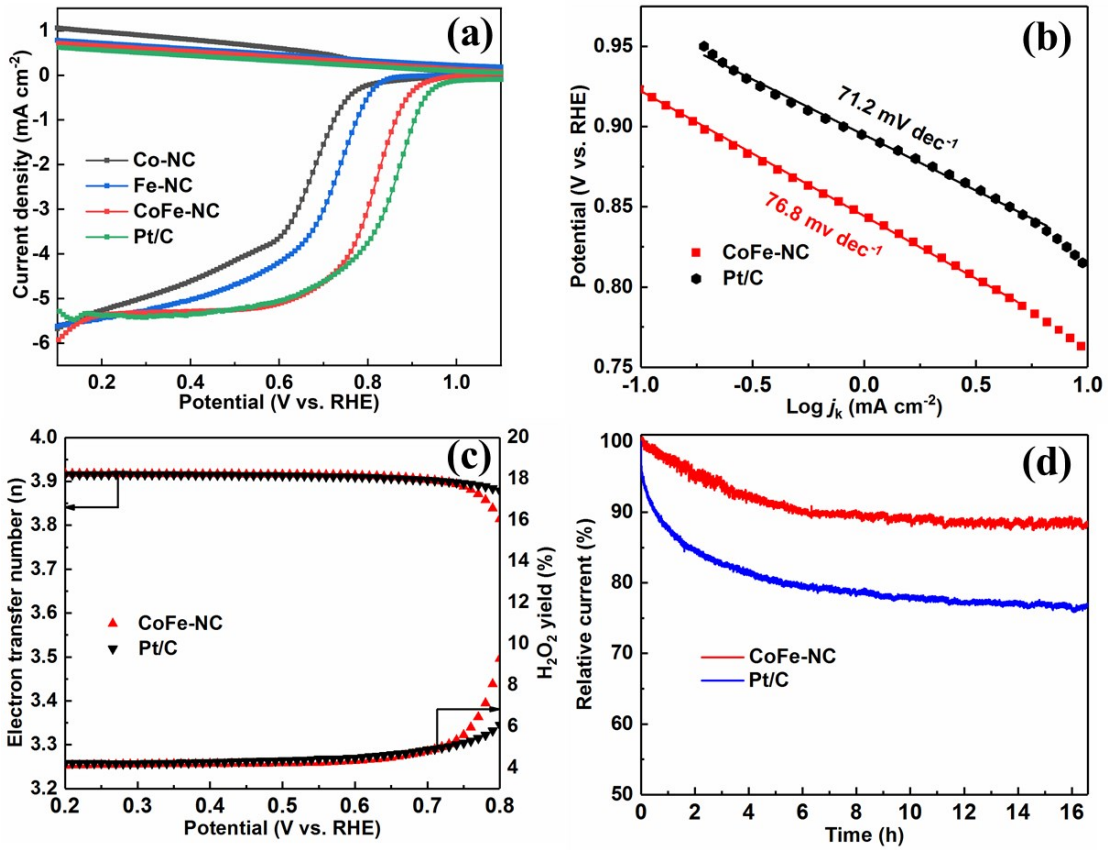


**Fig. S14.** The ORR performance in 0.1 M $HClO_4$. (a) LSV curves of Co-NC, Fe-NC, CoFe-NC, and Pt/C measured in $O_2$-saturated 0.1 M $HClO_4$ with a rotation rate of 1600 rpm, (b) Tafel plots of CoFe-NC and Pt/C, (c) the $H_2O_2$ yield and electron transfer numbers, (d) *i-t* curves of CoFe–NC and Pt/C at 0.8 V with 900 rpm.

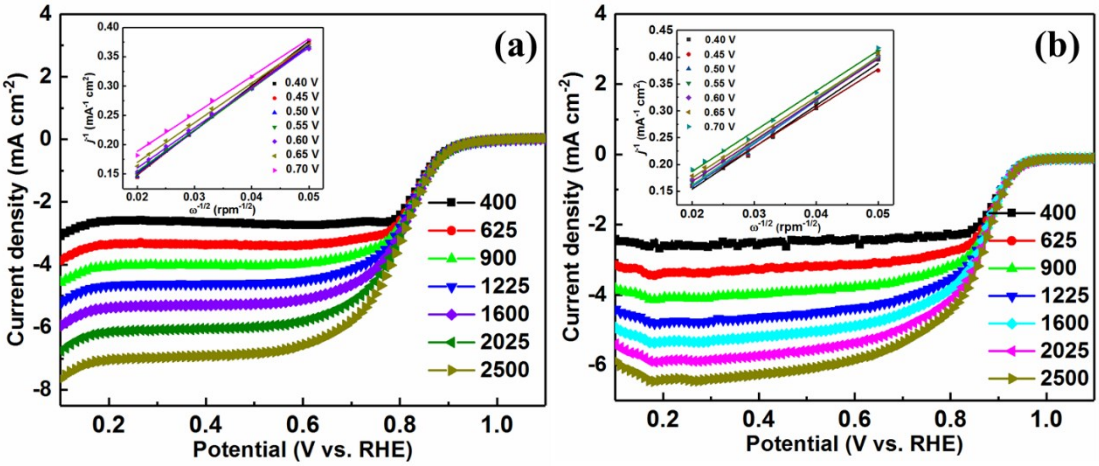


**Fig. S15**. The RDE polarization curves at different rotation rates and the inset is the corresponding K-L plots of CoFe-NC (a) and Pt/C (b) in 0.1 M $HClO_4$.

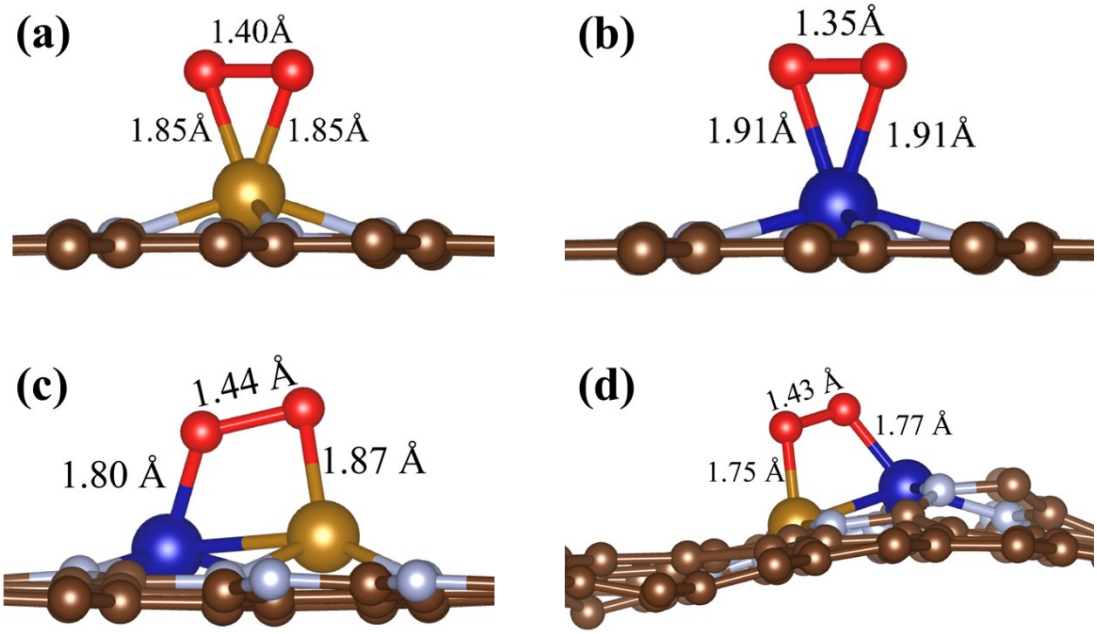


**Fig. S16** Side view of the optimized structures of $O_2$ molecule adsorbed on the (a) SA Fe, (b) SA Co, Co-Fe dimer sites on (c) the highly ordered NC substrate, and (d) the slightly disordered NC substrate. The O−O bond length, the Fe-O bond length, and the Co-O bond length are also labeled.

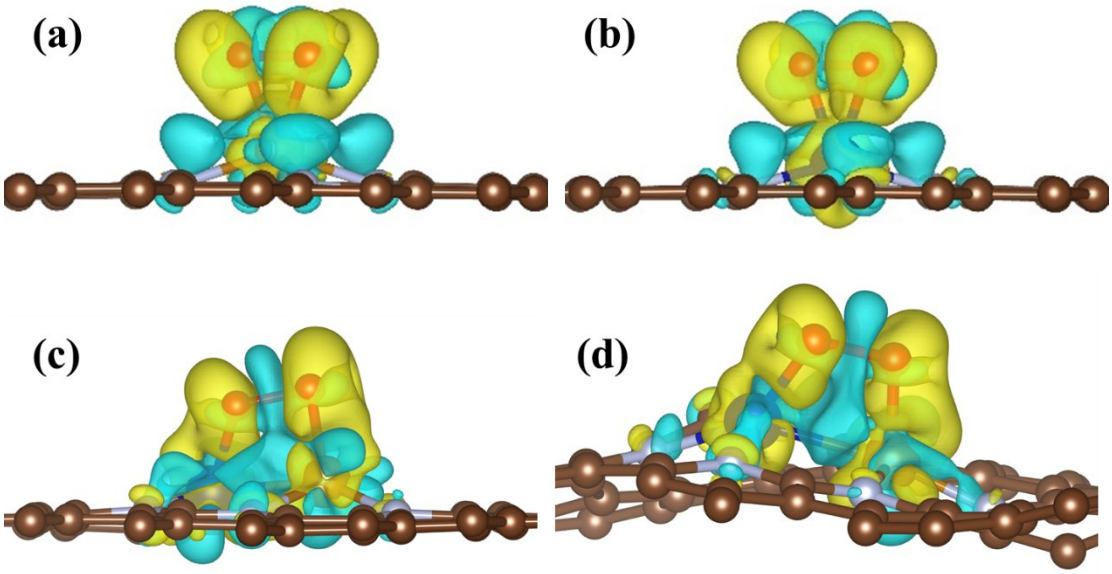


**Fig. S17.** Side view of charge density difference plot for $O_2$ molecule adsorbed on the different substrates, (a) SA Fe, (b) SA Co, (c) dual Fe-Co on the highly ordered NC substrate, (d) dual CoFe on the slightly disordered NC substrate. The yellow and blue regions indicate positive (charge accumulation) and negative (charge depletion) domains, respectively.

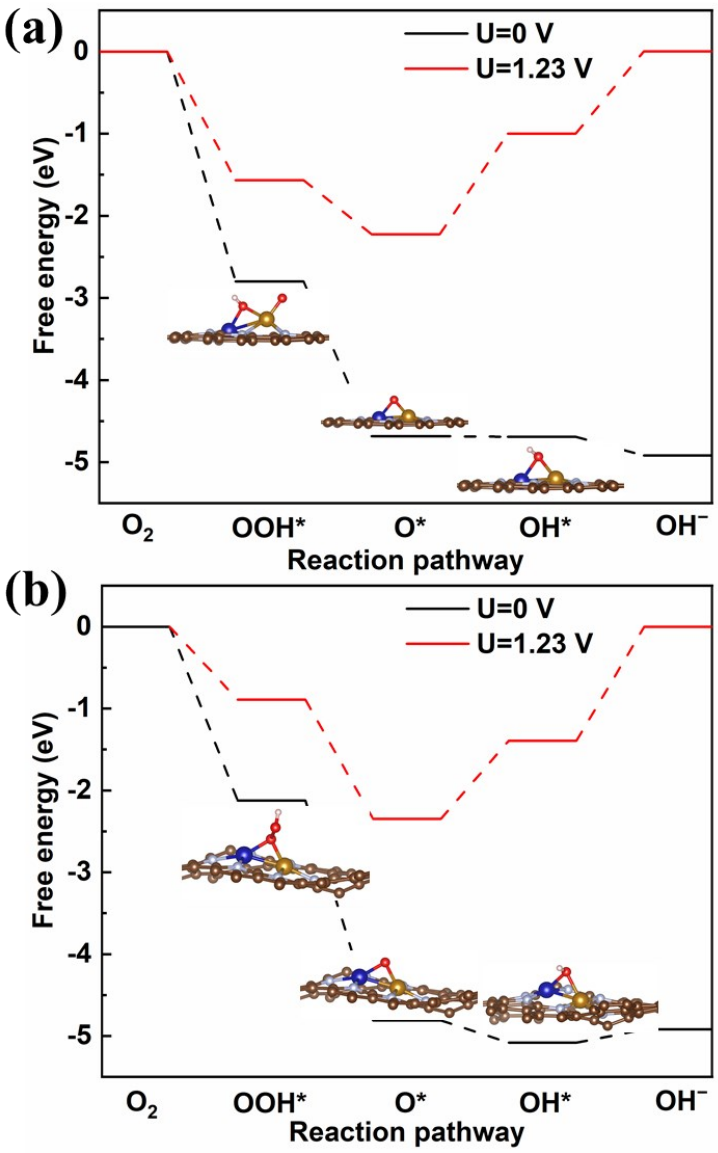


**Fig. S18.** Free energy diagram of ORR on CoFe-NC with highly ordered (a) and slightly disordered (b) NC substrate at U = 0 V and U = 1.23 V. The intermediates OOH*, O*, and OH* adsorbed on the substrate are shown inset of the figure.

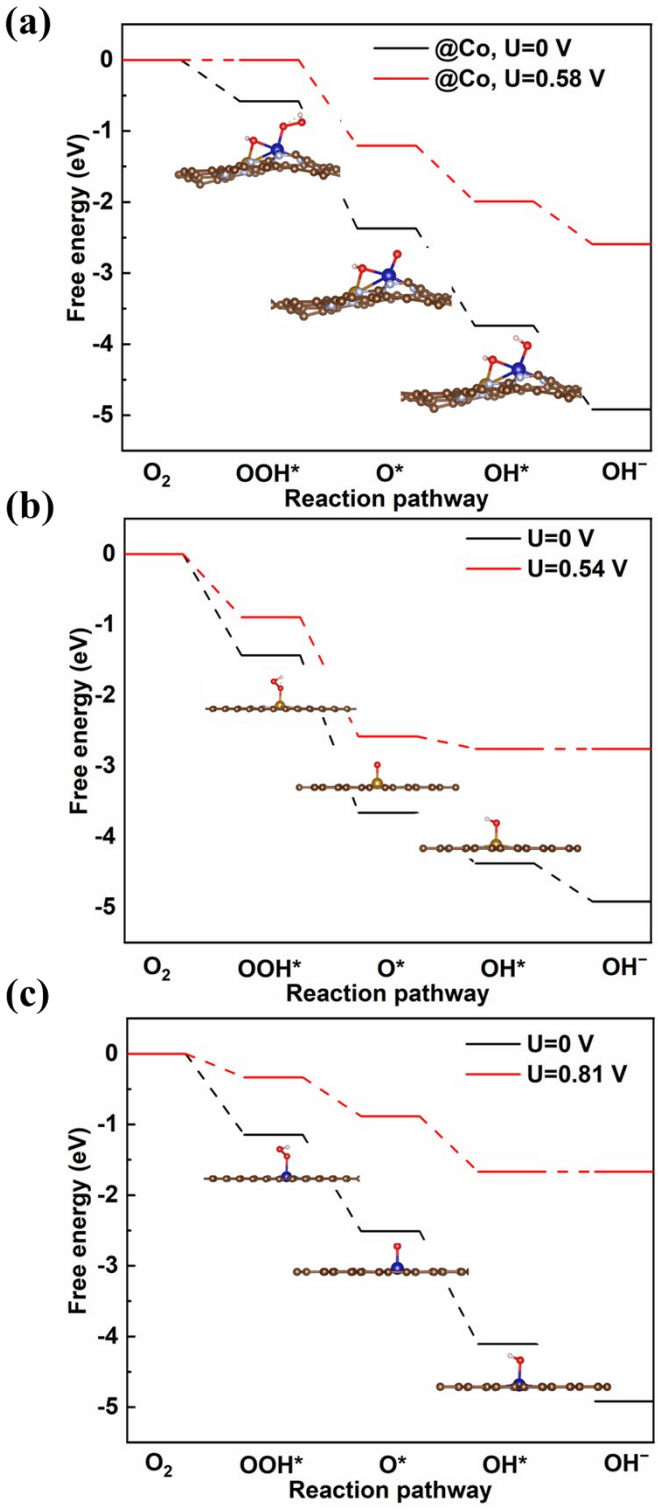


**Fig. S19** Free energy diagram of ORR (a) on the Co site of OH anchored dual CoFe on the slightly disordered NC substrate at U = 0 V and U = 0.58 V. (b) and (c) show the free energy diagram of ORR on the (b) Fe site of Fe-NC and on the (c) Co site of Co-NC. The intermediates OOH*, O*, and OH* adsorbed on the substrate are shown inset of the figure.

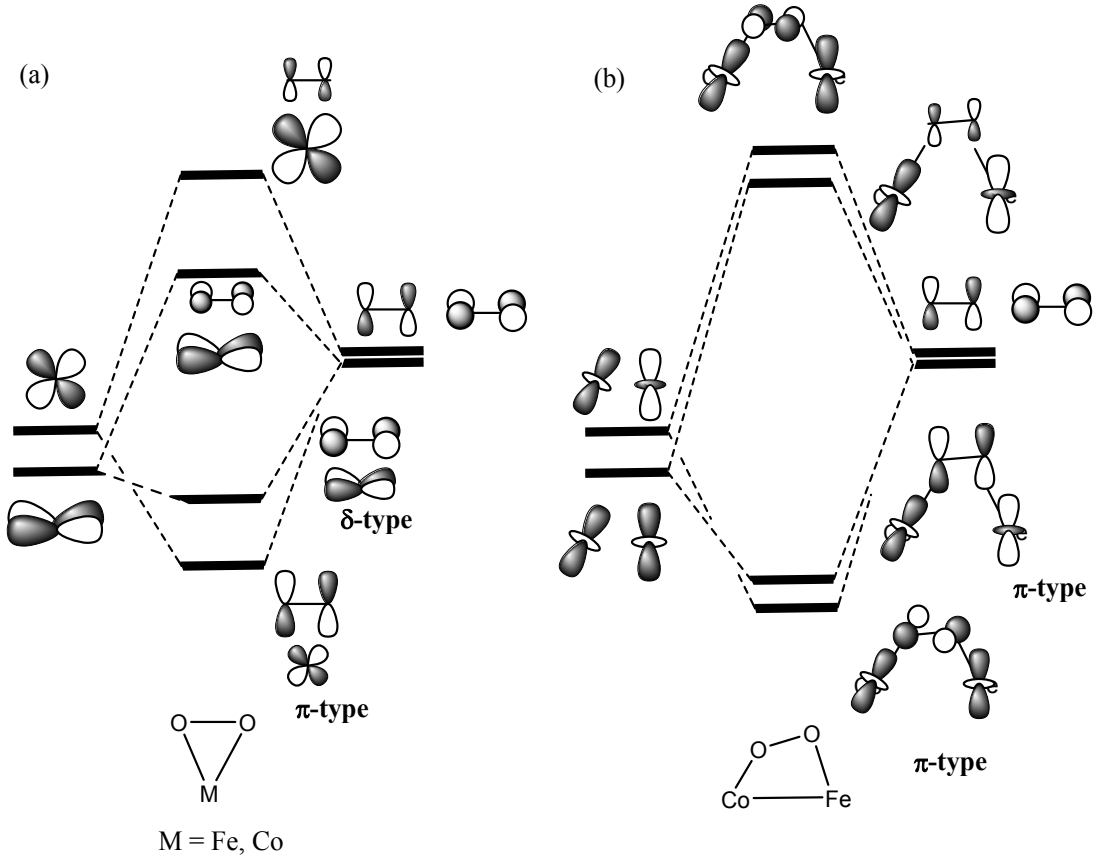


**Fig. S20** Schematic illustration of the molecular orbital interactions for (a) Fe SA or Co SA (b) Co-Fe dimers in the NC substrate with the adsorbate O2 (Only the transition metals and O2 were shown for simplicity).

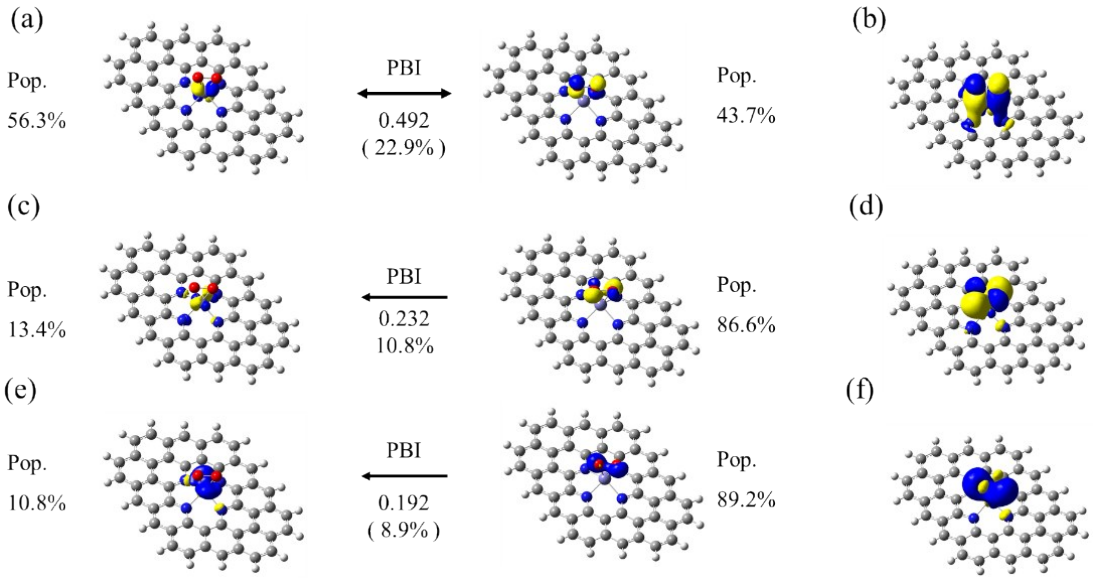


**Fig. S21** PISO analysis of the interactions between the SA Fe and $O_2$ for α electrons. (a) Dominant PISOs for the interaction across the Fe-$O_2$, consist of the $d_{yz}$ orbital of Fe and the p* orbital of $O_2$, contributes 22.9% interaction to the total interactions, the comparable population of the SA Fe and $O_2$ suggested the formation of chemical bonds (b) the formed p-type principal interacting molecular orbital (PIMO) which corresponds to the in-phase combinations of two PISO; (c) the second interactions between Fe and $O_2$, contributed by the $d_{xy}$ orbital of Fe and the other p* orbital of $O_2$; (d) the corresponding d-type PIMO; (e) the third principal interactions between Fe and $O_2$, consist of the s orbital of Fe and out-of-phase combinations of two s orbitals of oxygen (f) the corresponding PIMO. The populations (occupation numbers) are given as Pop near each PISO. The PIO-based bond indices (abbreviated as PBI) and its contribution (as %) to the total interactions between two fragments (the contributions of all PIOs sum up to 100%) are given near the arrow. Here, a large PBI indicated a stronger interaction, which also has a higher contribution to the total interactions.

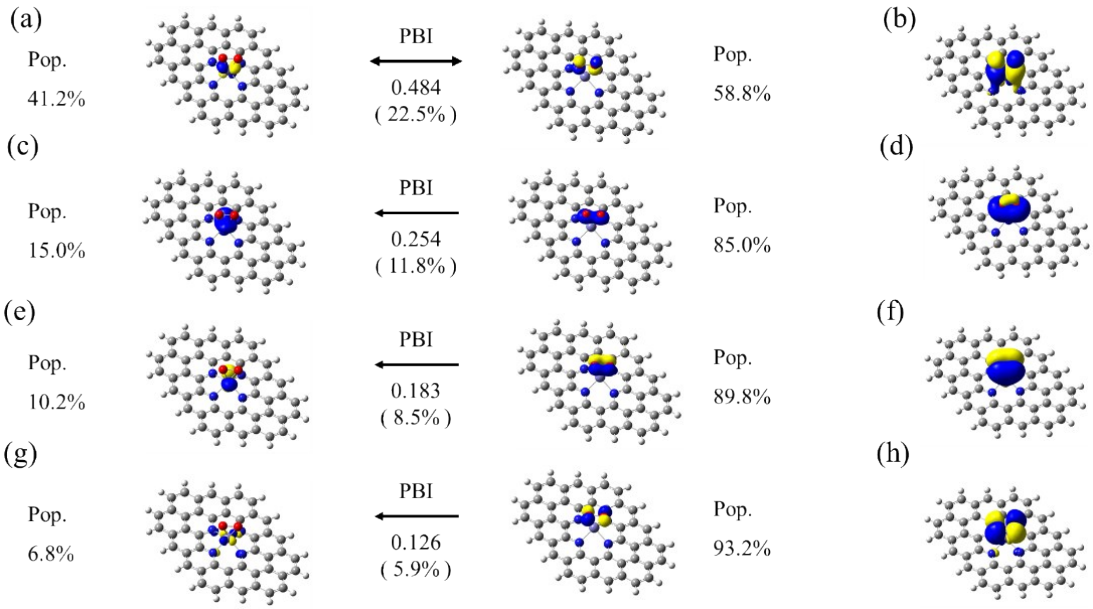


**Fig. S22** PISO analysis of the interactions between the SA Fe and $O_2$ for β electrons. (a) Dominant PISOs for the interaction across the Fe-$O_2$, consist of the $d_{xz}$ orbital of Fe and the p* orbital of $O_2$, contributes 22.5% interaction to the total interactions; (b) the formed p-type PIMO; (c) the secondary interactions between Fe and $O_2$, contributed by the s orbital of Fe and the in-phase combinations of two s orbitals of oxygen; (d) the corresponding s-type PIMO; (e) the third principal interactions between Fe and $O_2$, contributed by the $p_y$ orbital of Fe and one of the p orbital of $O_2$; (f) the corresponding p-type PIMO. (g) the fourth principal interactions between Fe and $O_2$, contributed by the $d_{xy}$ orbital of Fe and the other p* orbital of $O_2$; (h the corresponding d-type PIMO. The populations (occupation numbers) are given as Pop near each PISO. The PBI and its contribution (as %) to the total interactions between two fragments (the contributions of all PIOs sum up to 100%) are given near the arrow.

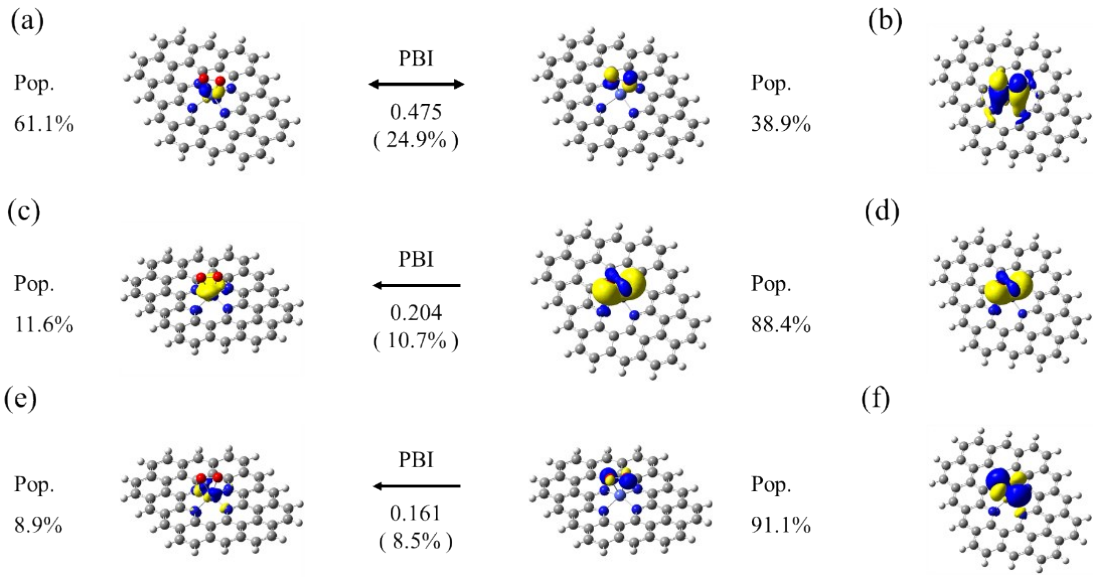


**Fig. S23** PISO analysis of the interactions between SA Co and $O_2$ for α electrons. (a) Dominant PISOs for the interaction across the Co-$O_2$, consist of the $d_{xz}$ orbital of Co and the p* orbital of $O_2$, contributes 24.9% interaction to the total interactions; (b) the formed p-type PIMO; (c) the secondary interactions between Co and $O_2$, consist of the s orbital of Co and in-phase combinations of two s orbitals of oxygen; (d) the corresponding PIMO; (e) the third principal interactions between Co and $O_2$, contributed by the $d_{xy}$ orbital of Co and the other p* orbital of $O_2$ (f) the corresponding d-type PIMO. The populations (occupation numbers) are given as Pop near each PISO. The PBI and its contribution (as %) to the total interactions between two fragments (the contributions of all PIOs sum up to 100%) are given near the arrow.

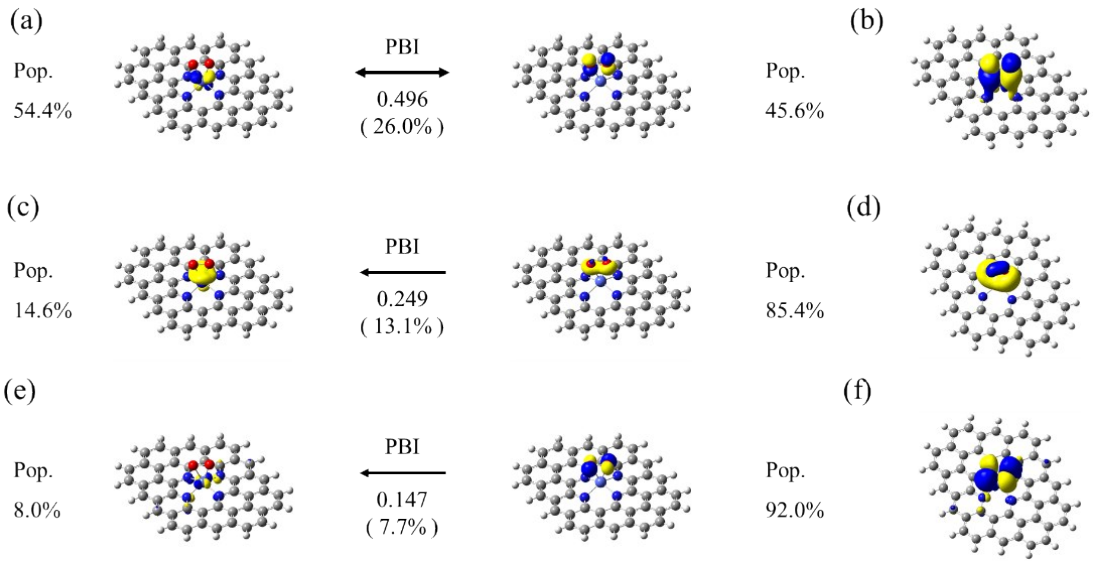


**Fig. S24** PISO analysis of the interactions between SA Co and $O_2$ for β electrons. (a) Dominant PISOs for the interaction across the Co-$O_2$, consist of the $d_{xz}$ orbital of Co and the p* orbital of $O_2$, contributes 26.0 % interaction to the total interactions; (b) the formed p-type PIMO; (c) the secondary principal interactions between Co and $O_2$, consist of the s orbital of Co and in-phase combinations of two s orbitals of oxygen; (d) the corresponding PIMO; (e) the third principal interactions between Co and $O_2$, contributed by the $d_{xy}$ orbital of Co and the other p* orbital of $O_2$ (f) the corresponding d-type PIMO. The populations (occupation numbers) are given as Pop near each PISO. The PBI and its contribution (as %) to the total interactions between two fragments (the contributions of all PIOs sum up to 100%) are given near the arrow.

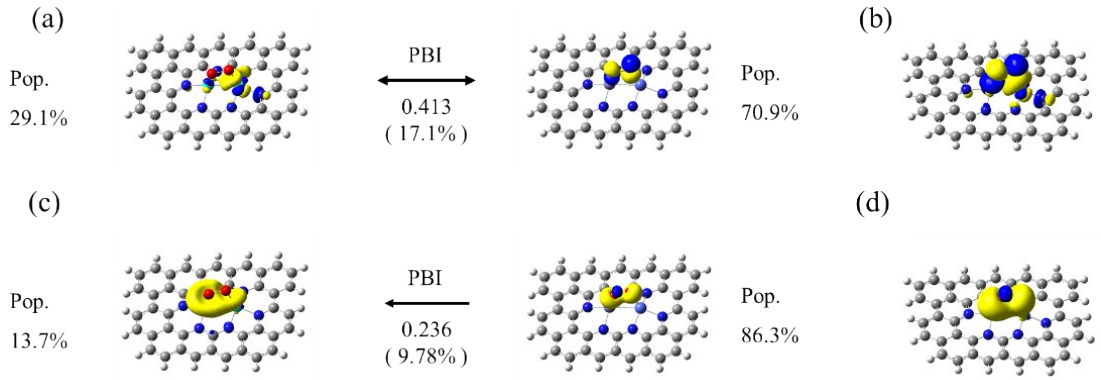


**Fig. S25** PISO analysis of the interactions between SA Co-Fe and $O_2$ for α electrons. (a) Dominant PISOs, consist of the $d_{z2}$ orbitals of Fe and Co as well as the p* orbital of $O_2$ (b) p* orbital of $O_2$ interacts with the out-of-phase combinations of $d_{z2}$ orbitals of Fe and Co to form p-type PIMO; (c) the secondary interactions between SA Co-Fe and $O_2$, consist of the in-phase combinations of s orbitals of Co, Fe and in-phase combinations of two s orbitals of oxygen; (d) the corresponding PIMO. The populations (occupation numbers) are given as Pop near each PISO. The PBI and its contribution (as %) to the total interactions between two fragments (the contributions of all PIOs sum up to 100%) are given near the arrow.

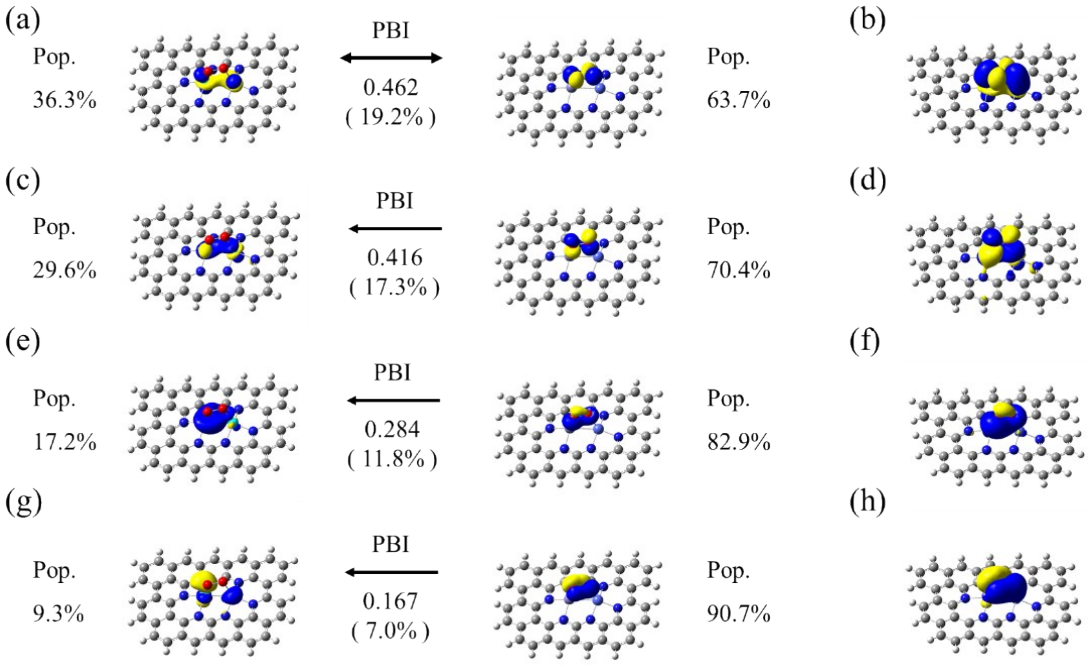


**Fig. S26** PISO analysis of the interactions between SA Fe-Co and $O_2$ for β electrons. (a) Dominant PISOs, consist of the $d_{z2}$ orbitals of Fe and Co as well as the p* orbital of $O_2$ (b) p* orbital of $O_2$ interacts with the in-phase combinations of $d_{z2}$ orbitals of Fe and Co to form p-type PIMO; (c) secondary PISOs, consist of the $d_{z2}$ orbitals of Fe and Co as well as the p* orbital of $O_2$ (d) p* orbital of $O_2$ interacts with the out-of-phase combinations of $d_{z2}$ orbitals of Fe and Co to form p-type PIMO; (e) the third principal interactions between SA Co-Fe and $O_2$, consist of the in-phase combinations of s orbitals of Co, Fe and in-phase combinations of two s orbitals of oxygen; (f) the corresponding PIMO; (g) the fourth principal interactions between SA Co-Fe and $O_2$, consist of the out-of-phase combinations of $d_{z2}$ orbitals of Fe and Co as well as the one p bond of $O_2$ (h) the corresponding PIMO. The populations (occupation numbers) are given as Pop near each PISO. The PBI and its contribution (as %) to the total interactions between two fragments (the contributions of all PIOs sum up to 100%) are given near the arrow.

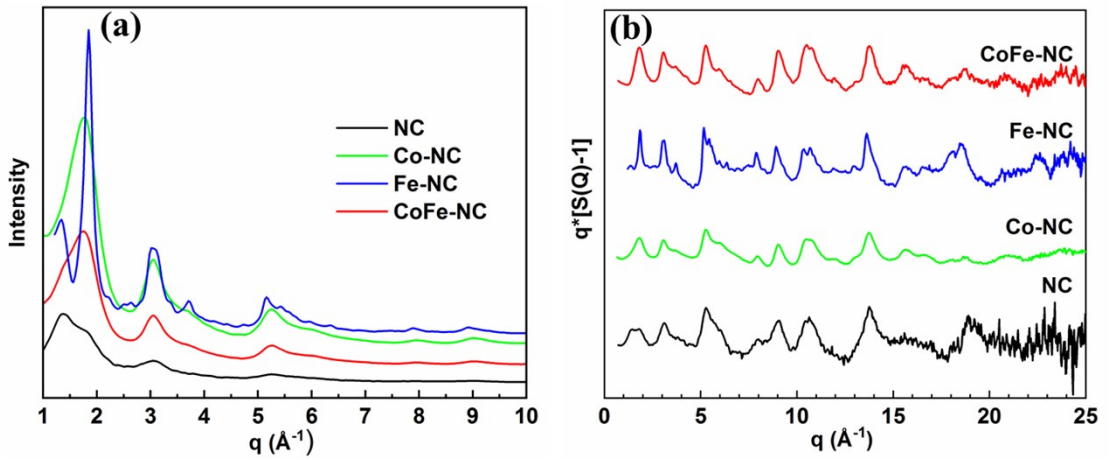


**Fig. S27** (a) High-energy X-ray diffraction (HE-XRD); (b) F(Q) transformation of the samples.

## Supplementary Tables

**Table S1**. Specific surface areas, total pore volume and pore distribution of OMC, NC, CoFe-C, and CoFe-NC.

| Sample | Sample description | Specific surface area ($m^2\ g^{-1}$) | Total pore volume ($cm^3\ g^{-1}$) | Pore size (nm) |
|---|---|---|---|---|
| OMC | PFR pyrolyzed at 900 °C without $NH_4Cl$ | 672 | 0.66 | Mainly distributed at 1.90~5.00 |
| NC | PFR pyrolyzed at 900 °C with $NH_4Cl$ | 810 | 1.28 | 1.69 |
| CoFe-C | CoFe/PFR pyrolyzed without $NH_4Cl$ | 767 | 1.11 | 1.86 |
| CoFe-NC | CoFe/PFR pyrolyzed with $NH_4Cl$ | 830 | 3.49 | 1.86 |

**Table S2**. Co, Fe contents analysis by XPS and ICP-AES for Co-NC, Fe-NC and CoFe-NC.

| Catalysts | XPS (wt.%) | | ICP-AES (wt.%) | |
|---|---|---|---|---|
| | Co | Fe | Co | Fe |
| Co-NC | 4.68 | - | 4.02 | - |
| Fe-NC | - | 4.37 | - | 3.80 |
| CoFe-NC | 3.39 | 2.15 | 2.88 | 1.90 |

**Table S3**. Bader charge analysis of the Fe, Co, and N atoms for the substrates with and without adsorbed $O_2$ molecule.

| Sample | Pure substrate | | | with adsorbed $O_2$ | | |
|---|---|---|---|---|---|---|
| | Fe | Co | N | Fe | Co | N |
| SA Fe | 1.14 | | -1.19 | 1.38 | | -1.17 |
| SA Co | | 0.90 | -1.18 | | 1.14 | -1.14 |
| Co-Fe on highly ordered NC substrate | 0.91 | 0.60 | -1.22 | 1.28 | 0.92 | -1.18 |
| Co-Fe on slightly disordered NC substrate | 0.91 | 0.61 | -1.24 | 1.13 | 0.88 | -1.22 |

**Table S4**. Co K-edge EXAFS data fitting results of samples.

| Sample | Shell | CN | NNDs (Å) | $\sigma^2$(Å$^2$) |
|---|---|---|---|---|
| Co-NC | Co-N | 2.74 ± 0.46 | 1.93 ± 0.01 | 0.005 |
| | Co-C1 | 4.66 ± 1.73 | 2.63 ± 0.04 | 0.005 |
| | Co-C2 | 5.04 ± 2.16 | 2.84 ± 0.04 | 0.005 |
| CoFe-NC | Co-N | 3.23 ± 0.46 | 1.85 ± 0.01 | 0.002 |
| | Co-Fe | 1.02 ± 0.21 | 2.07 ± 0.02 | 0.005 |

**Table S5**. Fe K-edge EXAFS data fitting results of samples.

| Sample | Shell | CN | NNDs (Å) | $\sigma^2$(Å$^2$) |
|---|---|---|---|---|
| Fe-NC | Fe-N | 4.86±0.58 | 2.00 ± 0.03 | 0.008 |
| | Fe-C1 | 5.63±0.76 | 2.56 ± 0.03 | 0.002 |
| | Fe-C2 | 4.70±1.27 | 3.00 ± 0.03 | 0.002 |
| CoFe-NC | Fe-N | 3.24 ± 0.48 | 1.94 ± 0.01 | 0.007 |
| | Co-Fe | 1.02 ± 0.21 | 2.07 ± 0.02 | 0.005 |

**Table S6**. Comparison of the ORR activity of the CoFe-NC catalyst with recently reported M-N-C in 0.1 M KOH and 0.1 M $HClO_4$ electrolyte.

| Catalysts | Scan rate ($mV\ s^{-1}$) | $E_{1/2}$ (V *vs*. RHE) | | $E_{onset}$ (V *vs*. RHE) | | Ref. |
|---|---|---|---|---|---|---|
| | | 0.1 M KOH | 0.1 M $HClO_4$ | 0.1 M KOH | 0.1 M $HClO_4$ | |
| CoFe-NC | 10 | 0.940 | 0.804 | 1.052 | 0.938 | This work |
| OM-NCNF-FeNx | 10 | 0.836 | - | 0.905 | - | [24] |
| Fe-NC HNS | 5 | 0.870 | - | 1.046 | - | [25] |
| N-Fe/G | 10 | 0.830 | - | 0.930 | - | [26] |
| Fe-ISAs/CN | 10 | 0.900 | 0.770 | 0.986 | 0.890 | [27] |
| $Fe_{SA}$-N-C | 10 | 0.891 | 0.776 | 1.000 | 0.900 | [28] |
| PCN-FeCo/C | 10 | 0.850 | 0.760 | 1.000 | 0.900 | [29] |
| f-FeCoNC900 | 5 | 0.890 | 0.810 | 1.050 | 0.870 | [30] |
| Fe, Mn-N/C-900 | 10 | 0.904 | - | 1.020 | - | [31] |
| CoPNi-N/C | 1 | 0.840 | 0.730 | 0.930 | 0.860 | [32] |
| (Zn,Co)/NSC | 10 | 0.893 | - | 1.070 | - | [33] |
| Zn/CoN-C | 5 | 0.861 | 0.796 | 1.004 | 0.97 | [34] |
| SA-Fe/NG | 5 | 0.880 | 0.800 | 1.000 | 0.900 | [35] |
| Co-SAs@NC | 5 | 0.820 | - | 0.960 | - | [36] |
| Fe-N-C-950 | 5 | - | 0.780 | - | 0.920 | [37] |
| CoNC-700 | 5 | 0.850 | 0.730 | 0.960 | 0.890 | [38] |
| Co-N-C-10 | 5 | - | 0.790 | - | 0.920 | [39] |
| Co SAs/N-C(900) | 10 | 0.881 | - | 0.982 | - | [40] |
| Cu-N-C | 5 | 0.869 | - | 0.920 | - | [41] |
| Zn-N-C-1 | 10 | 0.873 | 0.746 | 1.000 | 0.890 | [42] |
| Cu-$N_4$-C | 10 | 0.840 | - | 0.960 | - | [43] |

**Table S7**. Comparison of Zn-air batteries performances of CoFe-NC with recently reported electrocatalysts.

| Catalysts | Electrolyte | Peak power density (mW $cm^{-2}$) | Specific capacity (mA h $g^{-1}$) | Stability | Reference |
|---|---|---|---|---|---|
| CoFe-NC | 6 M KOH+0.2 M $Zn(OAc)_2$ | 115 | 791 at 10 mA $cm^{-2}$ | 10 min/cycle for 80 cycles at 10 mA $cm^{-2}$, without visible discharge voltage loss | This work |
| Co@C-N | 6 M KOH+0.2 M $Zn(OAc)_2$ | 105 | 741 at 10 mA $cm^{-2}$ | 20 min/cycle for 90 cycles at 10 mA $cm^{-2}$, voltage gap increased ~0.02 V | 44 |
| SA-Fe/NG | 6 M KOH+0.2 M $ZnCl_2$ | 91 | - | 40 min/cycle for 30 cycles at 10 mA $cm^{-2}$, no significant change | 35 |
| (Fe, Co)/CNT | 6 M KOH | 260 | 774 at 50 mA $cm^{-2}$ | - | 45 |
| Zn-N-C-1 | 6 M KOH | 179 | 683 at 100 mA $cm^{-2}$ | - | 42 |
| Co4N/CNW/CC | 6 M KOH+0.2 M $Zn(OAc)_2$ | 174 | 774 at 10 mA $cm^{-2}$ | 20 min/cycle for 408 cycles at 10 mA $cm^{-2}$, no visible change | 46 |
| Co-SAs@-NC | 6 M KOH+0.2 M $Zn(OAc)_2$ | 105 | 897 at 20 mA $cm^{-2}$ | 20 min/cycle for 255 cycles at 10 mA $cm^{-2}$, without visible voltage loss | 36 |
| Fe, Mn-N/C-900 | 6 M KOH+0.2 M $Zn(OAc)_2$ | 140 | - | Negligible change at 20 mA $cm^{-2}$ for 6.4 h | 31 |
| (Zn, Co)/NSC | 6 M KOH+0.2 M $ZnCl_2$ | 97 | - | Almost no voltage decay during test at 5 mA $cm^{-2}$ for 22 h | 33 |
| NC-Co SA | 6 M KOH+0.1 M $Zn(OAc)_2$ | ~ | ~ | 20 min/cycle for 180 h at 10 mA $cm^{-2}$, excellent stability | 47 |

## References


1. E. Gann, C. R. McNeill, A. Tadich, B. C. C. Cowie and L. Thomsen, *J. Synchrotron Radiat.*, 2016, **23**, 374-380.
2. B. Ravel and M. Newville, *J. Synchrotron Radiation*, 2005, **12**, 537-541.
3. L. A. Rochford, D. S. Keeble, O. J. Holmes, G. J. Clarkson and T. S. Jones, *J. Mater. Chem. C*, 2014, **2**, 6056-6060.
4. P. A. Reynolds, B. N. Figgis, E. S. Kucharski and S. A. Mason, *Acta Crystallograph. Sec. B*, 1991, **47**, 899-904.
5. O. Bunău and Y. Joly, *Journal of Physics: Condensed Matter*, 2009, **21**, 345501.
6. Y. Joly, *Physical Review B*, 2001, **63**, 125120.
7. S. A. Guda, A. A. Guda, M. A. Soldatov, K. A. Lomachenko, A. L. Bugaev, C. Lamberti, W. Gawelda, C. Bressler, G. Smolentsev, A. V. Soldatov and Y. Joly, *Journal of Chemical Theory and Computation*, 2015, **11**, 4512-4521.
8. V. Petkov, *Mater. Today*, 2008, **11**, 28-38.
9. V. Petkov, *J. Appl. Crystallography*, 1989, **22**, 387-389.
10. J. Liu, Z. Li, X. Zhang, K.-i. Otake, L. Zhang, A. W. Peters, M. J. Young, N. M. Bedford, S. P. Letourneau, D. J. Mandia, J. W. Elam, O. K. Farha and J. T. Hupp, *ACS Catal.*, 2019, **9**, 3198-3207.
11. G. Kresse and J. Furthmüller, *Phys. Rev. B*, 1996, **54**, 11169.
12. G. Kresse and J. Furthmüller, *Comput. Mater. Sci.*, 1996, **6**, 15-50.
13. P. E. Blöchl, *Phys. Rev. B*, 1994, **50**, 17953.
14. J. P. Perdew, K. Burke and M. Ernzerhof, *Phys. Rev. Lett.*, 1996, **77**, 3865-3868.
15. Z. Lu, B. Wang, Y. Hu, W. Liu, Y. Zhao, R. Yang, Z. Li, J. Luo, B. Chi, Z. Jiang, M. Li, S. Mu, S. Liao, J. Zhang and X. Sun, *Angew. Chem., Int. Ed.*, 2019, **58**, 2622-2626.
16. J. Wang, W. Liu, G. Luo, Z. Li, C. Zhao, H. Zhang, M. Zhu, Q. Xu, X. Wang, C. Zhao, Y. Qu, Y. Zhengkun, Y. Tao, L. Y. Li, L. Y. Lin, W. Yuen and L. Yadong, *Energy Environ. Sci.*, 2018, **11**, 3375-3379.
17. Y. Chen, S. Ji, S. Zhao, W. Chen, J. Dong, W.-C. Cheong, R. Shen, X. Wen, L. Zheng, A. I. Rykov, S. Cai, H. Tang, Z. Zhuang, C. Chen, Q. Peng, D. Wang and Y. Li, *Nat. Commun.*, 2018, **9**, 5422.
18. M. Frisch, G. W. Trucks, H. B. Schlegel, G. E. Scuseria, M. A. Robb, J. R. Cheeseman, G. Scalmani, V. Barone, B. Mennucci and G. e. Petersson, 2014.
19. J. X. Zhang, F. K. Sheong and Z. Lin, *Chem. Eur. J.*, 2018, **24**, 9639-9650.
20. P. J. Hay and W. R. Wadt, *J. Chem. Phys.*, 1985, **82**, 270-283.
21. G. Igel-Mann, H. Stoll and H. Preuss, *Mol. Phys.*, 1988, **65**, 1321-1328.
22. D. Andrae, U. Haeussermann, M. Dolg, H. Stoll and H. Preuss, *Theoret. Chim. Acta*, 1990, **77**, 123-141.
23. J. K. Nørskov, J. Rossmeisl, A. Logadottir, L. Lindqvist, J. R. Kitchin, T. Bligaard and H. Jónsson, *J. Phys. Chem. B*, 2004, **108**, 17886-17892.
24. C. Cheng, S. Li, Y. Xia, L. Ma, C. Nie, C. Roth, A. Thomas and R. Haag, *Adv. Mater.*, 2018, **30**, 1802669.
25. Y. Chen, Z. Li, Y. Zhu, D. Sun, X. Liu, L. Xu and Y. Tang, *Adv. Mater.*, 2019, **31**, 1806312.
26. J. Wang, H. Zhang, C. Wang, Y. Zhang, J. Wang, H. Zhao, M. Cheng, A. Li and J. Wang,

*Energy Storage Mater.*, 2018, **12**, 1-7.

27. Y. Chen, S. Ji, Y. Wang, J. Dong, W. Chen, Z. Li, R. Shen, L. Zheng, Z. Zhuang, D. Wang and Y. Li, *Angew. Chem. Int. Ed.*, 2017, **129**, 7041-7045.
28. L. Jiao, G. Wan, R. Zhang, H. Zhou, S. H. Yu and H. L. Jiang, *Angew. Chem. Int. Ed.* , 2018, **57**, 8525-8529.
29. Q. Lin, X. Bu, A. Kong, C. Mao, F. Bu and P. Feng, *Adv. Mater.*, 2015, **27**, 3431-3436.
30. G. Zhang, Y. Jia, C. Zhang, X. Xiong, K. Sun, R. Chen, W. Chen, Y. Kuang, L. Zheng, H. Tang, W. Liu, J. Liu, X. Sun, W.-F. Lin and H. Dai, *Energy Environ. Sci.*, 2019, **12**, 1317-1325.
31. S. Gong, C. Wang, P. Jiang, L. Hu, H. Lei and Q. Chen, *J. Mater. Chem. A*, 2018, **6**, 13254-13262.
32. Z. Li, H. He, H. Cao, S. Sun, W. Diao, D. Gao, P. Lu, S. Zhang, Z. Guo and M. Li, *Appl. Catal. B Environ.*, 2019, **240**, 112-121.
33. D. Liu, B. Wang, H. Li, S. Huang, M. Liu, J. Wang, Q. Wang, J. Zhang and Y. Zhao, *Nano Energy*, 2019, **58**, 277-283.
34. Z. Lu, B. Wang, Y. Hu, W. Liu, Y. Zhao, R. Yang, Z. Li, J. Luo, B. Chi and Z. Jiang, *Angew. Chem.* , 2019, **131**, 2648-2652.
35. L. Yang, D. Cheng, H. Xu, X. Zeng, X. Wan, J. Shui, Z. Xiang and D. Cao, *Proc. Natl. Acad. Sci. U. S. A.*, 2018, **115**, 6626.
36. X. Han, X. Ling, Y. Wang, T. Ma, C. Zhong, W. Hu and Y. Deng, *Angew. Chem. Int. Ed.*, 2019, **58**, 5359-5364.
37. M. Xiao, J. Zhu, L. Ma, Z. Jin, J. Ge, X. Deng, Y. Hou, Q. He, J. Li, Q. Jia, S. Mukerjee, R. Yang, Z. Jiang, D. Su, C. Liu and W. Xing, *ACS Catal.*, 2018, **8**, 2824-2832.
38. G. Wan, P. Yu, H. Chen, J. Wen, C.-j. Sun, H. Zhou, N. Zhang, Q. Li, W. Zhao, B. Xie, T. Li and J. Shi, *Small*, 2018, **14**, 1704319.
39. M. Xiao, H. Zhang, Y. Chen, J. Zhu, L. Gao, Z. Jin, J. Ge, Z. Jiang, S. Chen, C. Liu and W. Xing, *Nano Energy*, 2018, **46**, 396-403.
40. P. Yin, T. Yao, Y. Wu, L. Zheng, Y. Lin, W. Liu, H. Ju, J. Zhu, X. Hong, Z. Deng, G. Zhou, S. Wei and Y. Li, *Angew. Chem.*, 2016, **128**, 10958-10963.
41. F. Li, G.-F. Han, H.-J. Noh, S.-J. Kim, Y. Lu, H. Y. Jeong, Z. Fu and J.-B. Baek, *Energy Environ. Sci.*, 2018, **11**, 2263-2269.
42. J. Li, S. Chen, N. Yang, M. Deng, S. Ibraheem, J. Deng, J. Li, L. Li and Z. Wei, *Angew. Chem.*, 2019, **131**, 7109-7113.
43. W. Li, C. Min, F. Tan, Z. Li, B. Zhang, R. Si, M. Xu, W. Liu, L. Zhou, Q. Wei, Y. Zhang and X. Yang, *ACS nano*, 2019, **13**, 3177-3187.
44. H. Yan, X. Zhao, N. Guo, Z. Lyu, Y. Du, S. Xi, R. Guo, C. Chen, Z. Chen, W. Liu, C. Yao, J. Li, S. J. Pennycook, W. Chen, C. Su, C. Zhang and J. Lu, *Nat. Commun.*, 2018, **9**, 3197.
45. J. Wang, W. Liu, G. Luo, Z. Li, C. Zhao, H. Zhang, M. Zhu, Q. Xu, X. Wang, C. Zhao, Y. Qu, Z. Yang, T. Yao, Y. Li, Y. Lin, Y. Wu and Y. Li, *Energy Environ. Sci.*, 2018, **11**, 3375-3379.
46. F. Meng, H. Zhong, D. Bao, J. Yan and X. Zhang, *J. Am. Chem. Soc.*, 2016, **138**, 10226-10231.
47. W. Zang, A. Sumboja, Y. Ma, H. Zhang, Y. Wu, S. Wu, H. Wu, Z. Liu, C. Guan, J. Wang and S. J. Pennycook, *ACS Catal.*, 2018, **8**, 8961-8969.